

DIELECTRIC BARRIER DISCHARGE FLOW CONTROL AT VERY LOW FLIGHT REYNOLDS NUMBERS

D. Greenblatt,^{*} B. Göksel,[†] C.Y. Schüle,^{*} C.O. Paschereit^{*}

^{*}Institute of Fluid Dynamics and Engineering Acoustics
Berlin University of Technology, Berlin, Germany

[†]Electrofluidsystems Ltd., Berlin, Germany

ABSTRACT

Experiments were performed on a flat plate airfoil and semi-span wing ($AR=6$) at very low flight Reynolds numbers ($3,000 \leq Re \leq 20,000$), where a dielectric barrier discharge plasma actuator was employed at the leading-edge to effect flow control. The actuator was driven in a high frequency (kHz) “steady” mode and a pulsed mode where pulse frequency and duty cycle were varied in a systematic fashion. Optimum reduced frequencies for generating post-stall lift were $O(0.5)$, which was broadly consistent with zero mass-flux slot-blowing data acquired at Reynolds numbers some 200 times higher. Nevertheless, profound differences in the response to reduced frequency and duty cycle were observed between the present tests and those conducted previously on an Eppler flying wing airfoil. Actuation produced considerable performance improvements, including an increase in maximum lift coefficient of 0.4 and maintained elevated endurance at significantly higher lift coefficients. These performance improvements did not diminish with actuation applied to the semi-span wing. Actuation in the “steady” mode resulted in effective boundary layer control up to 26 degrees angle of attack and thrust was developed at $Re < 9,000$. Actuation also exerted a significant effect on the wake at pre-stall angles of attack, where control of the upper surface bubble shedding produced significant differences in wake spreading and vortex shedding.

1. INTRODUCTION

Achieving sustained flight of micro air vehicles (MAVs) brings significant challenges due to their small dimensions and low flight speeds. [1] For so-called mini air vehicles, that operate in the $100,000 < Re < 300,000$ range, efficient systems can be designed by managing boundary layer transition via tripping at multiple locations. [2] However, at Reynolds numbers routinely experienced by MAVs ($Re < 100,000$), conventional low-Reynolds-number airfoils perform poorly, or even generate no useful lift. Some of the best performing airfoils in this Re range are cambered flat plates and airfoils with a thickness-to-chord ratio (t/c) of approximately 5%. [1] There are various definitions for MAV dimensions and weight, although one common definition refers to so-called “large” ($b=15\text{cm}$, $M=90\text{g}$) and “small” ($b=8\text{cm}$, $M=30\text{g}$) MAVs. [1] In order to maximize wing area, these vehicles typically have low aspect ratio wings ($1 \leq AR \leq 2$) where typical Reynolds numbers during loiter are in the range $20,000 < Re < 80,000$, based on the abovementioned specifications. Innovative designs with larger aspect ratio wings (cf. [2]) result in an even lower Reynolds number range.

The challenge of developing useful lift intensifies with yet smaller vehicles required to fly at even lower flight speeds. [10] This includes the development of so-called nano-UAVs whose missions include flying within confined areas. These are commonly termed Nano Air Vehicles (NAVs), and are defined as weighing less than 10g with dimensions smaller than $\sim 7.5\text{cm}$ and speeds between 0.5 and $\sim 7.5\text{m/s}$. [3] The significant difficulty associated with

generating lift at $Re < 20,000$ has led many to pursue so-called biologically inspired approaches, where the flight of small birds and insects is mimicked to a greater or lesser degree.

In contrast to these approaches, the objective of the present investigation is to study “conventional” active flow concepts on wings and airfoils at Reynolds numbers that are typical of small MAVs and NAVs. This has been achieved using a so-called dielectric barrier discharge (DBD) actuator, [4,5,6] typically driven in the 3kHz to 10kHz frequency range. The actuator was calibrated for both pulsed and non-pulsed “steady” actuation modes. For the purposes of this study, a “flat-plate” airfoil was subjected to active control for the range $3,000 \leq Re \leq 20,000$. The plate performance was also tested as a semi-span wing ($AR=6$). A previous investigation on the Eppler E338 airfoil revealed that separation moves upstream with increasing angle of attack from $x/c \sim 30\%$ at $\alpha=0^\circ$ to the leading-edge at $\alpha \sim 25^\circ$. Selection of the relatively simple flat plate avoided this problem, thereby ensuring that the separation point would always be fixed at the leading-edge and thus the relative position of separation to actuation would remain constant. An additional motivation for using this simple geometry was to generate a data set that could be used to validate theoretical or computational approaches. Even though the introduction of camber improves baseline (uncontrolled) performance [1], it was not introduced in this investigation due to our desire to initially eliminate surface curvature as a parameter. Parametric studies, based on the measurement of aerodynamic loads, were carried out in order to establish the optimum reduced frequencies, minimum duty cycle and minimum power input required to maintain or maximize performance. Data acquired during the parametric study was complemented by smoke-wire flow visualization. Selected data from an associated study on an Eppler E338 airfoil [6] was compared with the present data set.

2. ACTUATOR CALIBRATION

Calibrating plasma actuators in-situ, i.e. determining the momentum generated in the presence of a free-stream, is not as straightforward as traditional boundary layer control involving the use of a slot for example. [7,8,9] In the absence of a free-stream, the plasma actuator draws fluid from quiescent surroundings giving rise to an effectively steady (3-10 kHz) wall jet. However, when the actuator is driven in a pulsed mode, the wall jet is comprised of steady and significant coherent unsteady components. With a free-stream present, the flow in the vicinity of the actuator is more complex, and the velocity at the edge of the boundary layer changes with the free-stream and angle of attack. Thus the net momentum added to the flow by the actuator in the absence of a free-stream flow will decrease. When the edge velocity reaches some threshold that is larger than that of the plasma jet, the near-wall momentum is depleted. A similar phenomenon was first recognized during the deployment of steady slot blowing where low steady jets had a deleterious effect on airfoil performance. [10]

For purposes of this investigation, the actuator was calibrated using an LDA in a quiescent environment ($U_\infty=0$), on the lower wall of a wind tunnel. The tunnel test section was seeded uniformly with $1\mu\text{m}$ diameter oil droplets. For active flow control studies, we are primarily interested in the mean and oscillatory components of momentum. Specifically, the calibration was performed for duty cycles between 1% and 100%. For “steady” actuation the actuator was driven at 4kHz (at 10kV peak-to-peak) and for pulsed (or unsteady) actuation, the wave modulation method was employed where the 4kHz carrier wave was modulated by a square-wave at the frequency f_m that corresponded to the reduced frequency range $0.1 \leq F^+ \leq 10$ ($F^+ \equiv f_m X_{te} / U_\infty$, where X_{te} is the distance from the actuator to the airfoil trailing-edge. [7], [8]).

This introduces mean (u_J) and unsteady (u'_J and v'_J) velocity components and thus the jet momentum is made up of time-mean and oscillatory component quantified by

$$J_{\text{tot}} = J + \langle J \rangle = \int_0^\infty \rho u_J^2 dy + \int_0^\infty \rho (u_J'^2 + v_J'^2) dy, \quad (1)$$

where the first term represents the steady contribution and the second term represents the oscillatory contribution. The total momentum coefficient is defined as

$$C_{\mu,\text{tot}} \equiv J_{\text{tot}} / q_\infty c = C_\mu + \langle C_\mu \rangle \quad (2)$$

from equation (1) and also expressed as ($C_\mu, \langle C_\mu \rangle$). [7] The high frequency (4kHz) actuation was modulated in the range of 2.5 to 100 Hz and the duty cycle (DC) was varied from 1% to 100%.

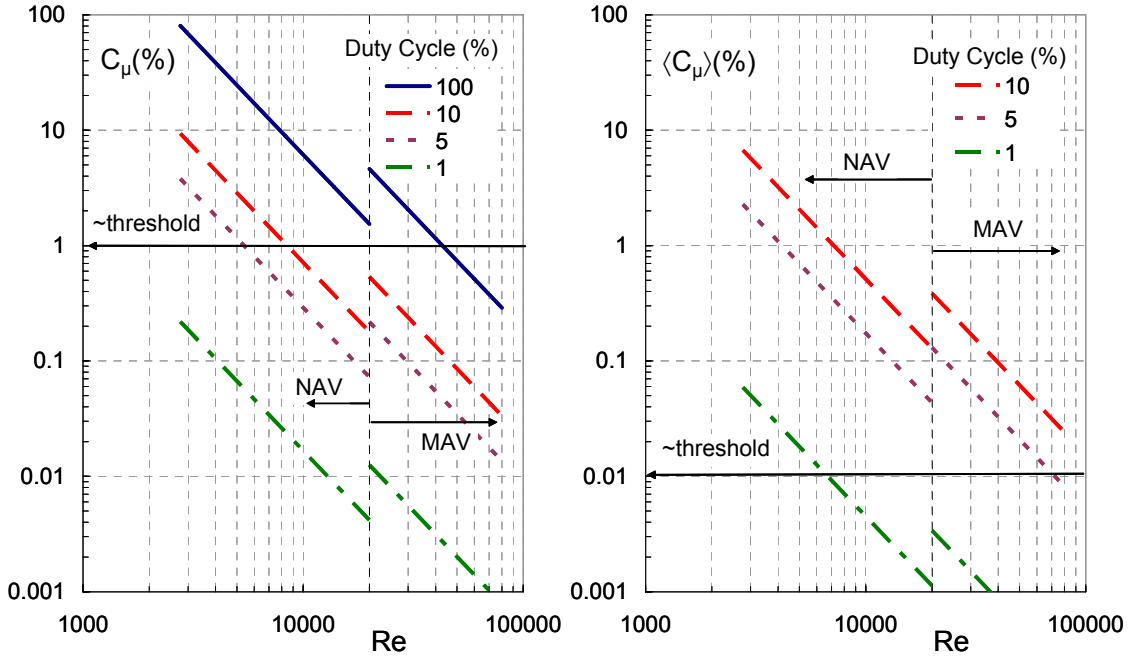


Fig. 1. Calibrated (a) steady and (b) oscillatory components of the momentum coefficient based on DBD actuator calibration. Assumed chord lengths of the MAV and NAV ranges are 15cm and 5cm respectively.

To illustrate the applicability of the DBD actuator, J and $\langle J \rangle$ were non-dimensionalized with respect to typical MAV and NAV dimensions, $c=15\text{cm}$ and 5cm , respectively. A U_∞ range was then selected to represent typical MAV and NAV Re ranges, and the results are shown in figs. 1a and 1b, for C_μ and $\langle C_\mu \rangle$ respectively. All data shown are for a quiescent calibration $U_\infty=0$; the calibration values were lower with $U_\infty>0$ [6] and thus the data presented here can be considered to be the upper limit of the momentum coefficients. Moreover, both coherent (periodic) and incoherent (turbulent) components are lumped in the unsteady terms.

On the abscissas a demarcation between NAV and MAV Reynolds numbers is made, based on [1], and although this demarcation is somewhat subjective, it is employed here for illustrative purposes. On the ordinates, the approximate thresholds above which control becomes effective are shown. It is well known that a threshold $\langle C_\mu \rangle$ can be two orders of magnitude less than that for C_μ and this is reflected in fig. 1b. For application to these low Reynolds number flows, the threshold values should be considered mainly as indicators, as they are applicable to conventional low Reynolds number flows. [7,8] Fig. 1a shows that in almost all cases, “steady” plasma jets do not cross the threshold for effective boundary layer control for typical MAVs. The only exception is for 100% duty cycle at $Re < 30,000$. For NAV Reynolds numbers, steady boundary layer control can be expected for all duty cycles of 5% and greater. Particularly, at low Reynolds numbers, around $Re < 10,000$, the C_μ available is comparable with that of circulation control at conventional low Reynolds numbers. [9] Note that at this point, no attention has been paid to the power requirements of the actuation.

In contrast to steady actuation, momentum produced as a result of pulsed actuation, for $DC \geq 5\%$, well exceeds the threshold necessary for effective MAV control. At NAV Reynolds numbers the control authority clearly increases and even $DC = 1\%$ can be expected to deliver some effect at approximately $Re < 7,000$.

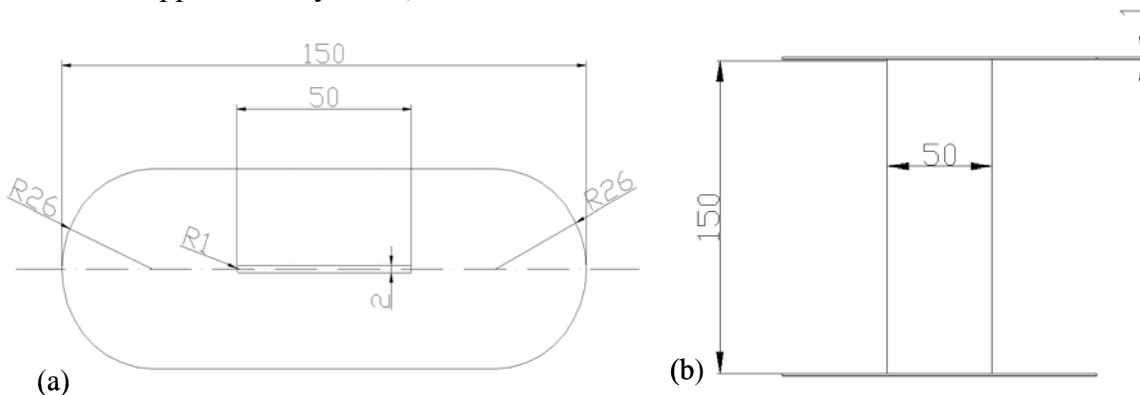


Fig. 2. Schematic of the experimental setup, showing (a) the flat plate location between the two oval end plates; and (b) a top view of the airfoil. The lower plate shown in (b) could be removed to produce a semi-span wing ($AR=6$).

3. EXPERIMENTAL SETUP

The measurements were conducted in an open section wind tunnel (400mm \times 280mm) of blow-down design, driven by a radial blower, with a 0.8 to 10 m/s velocity range. An aluminium, bending beam strain gauge-type balance (3-component) was designed and constructed for the measurement of forces and moments in the Reynolds number range $3,000 < Re < 200,000$. A variable length sting was used to facilitate measurable forces corresponding to the large variation in load range. Experiments were performed on a “flat plate” airfoil, that was mounted between oval endplates (see figs. 2a and 2b). The balance was mounted on top of the wind tunnel and the wing was attached vertically to the balance by means of the sting.

The “airfoil” was a 2mm thick rectangular flat plate with a 50 mm chord length and 150mm span, made of plywood and covered with epoxy that was sandpapered and polished. The leading-edge was circular with a 1mm radius and the trailing-edge was blunt (a previous investigation found very little effect of the trailing edge radius variation [1]). For 2D

measurements, two endplates made from 1mm thick Plexiglas were fixed at both ends; for 3D measurements, the lower endplate was removed producing $AR=6$ (semi-span $AR=3$).

Data generated using the aforementioned setup was compared with the flat plate wing data of Schmitz [11], that had a similar aspect ratio, and is shown in figs. 3a and 3b. The C_l versus α slopes are similar, possibly due to the combined effect of higher Re and slightly smaller aspect ratio in the case of Schmitz [11]. The zero lift drag coefficient increases substantially with decreasing Re mainly due to the increasing viscous component where $C_D \sim Re^{-1/2}$.

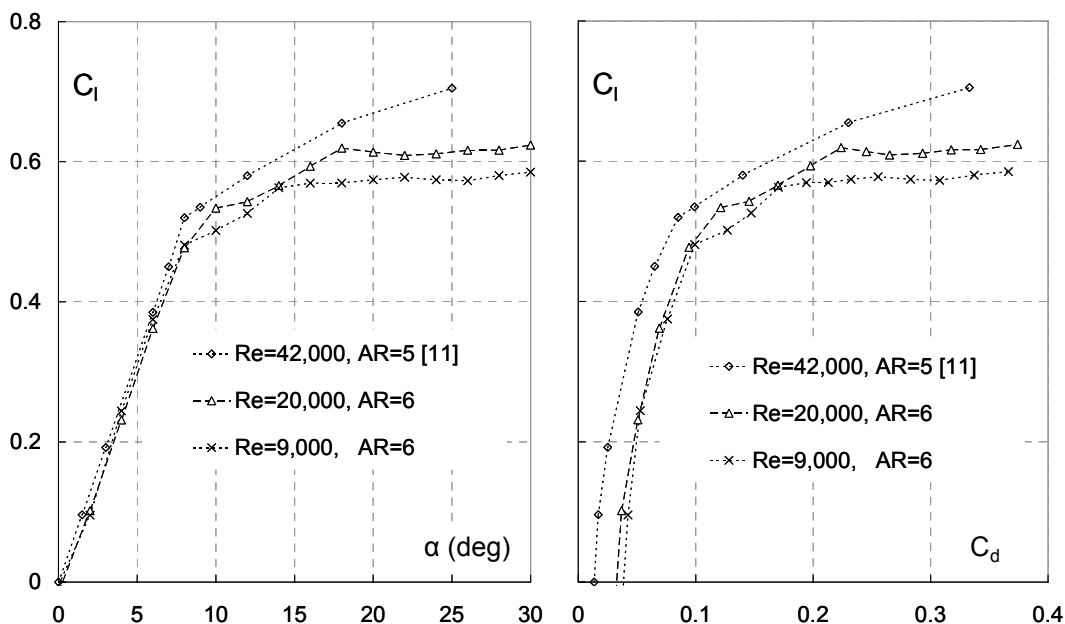


Fig. 3: Comparison of lift and drag coefficient data acquired on the semi-span wing (lower endplate removed in fig. 2b) with the wing of Schmitz. [11]

4. DISCUSSION OF RESULTS

For a given application, in this case performance enhancement at very low flight Reynolds numbers, a comprehensive optimization study should consider two separate, but related, aspects of the problem. The first has to do with strictly aerodynamic aspects, e.g. optimum actuator placement, optimum F^+ or minimum $\langle C_{\mu} \rangle$, and hence power, for which performance is maintained or improved. The second has to do with specifics of the actuator design, including electrodes and dielectric properties (thickness and dielectric coefficient) and the driving electronics utilized for generating the plasma. Here attention must be paid to various power losses, for example due to reactive power, dielectric heating and those due to plasma maintenance power [12]. In the present work, mainly the aerodynamic aspects were considered while actuator design aspects were not addressed. Consequently, no optimization studies were performed to reduce losses due to reactive power by impedance matching the high frequency power supply to the plasma actuator. The losses due to dielectric heating and maintenance power were kept to a minimum by driving the plasma with lower ionization frequencies still sufficient to ignite a glow discharge.

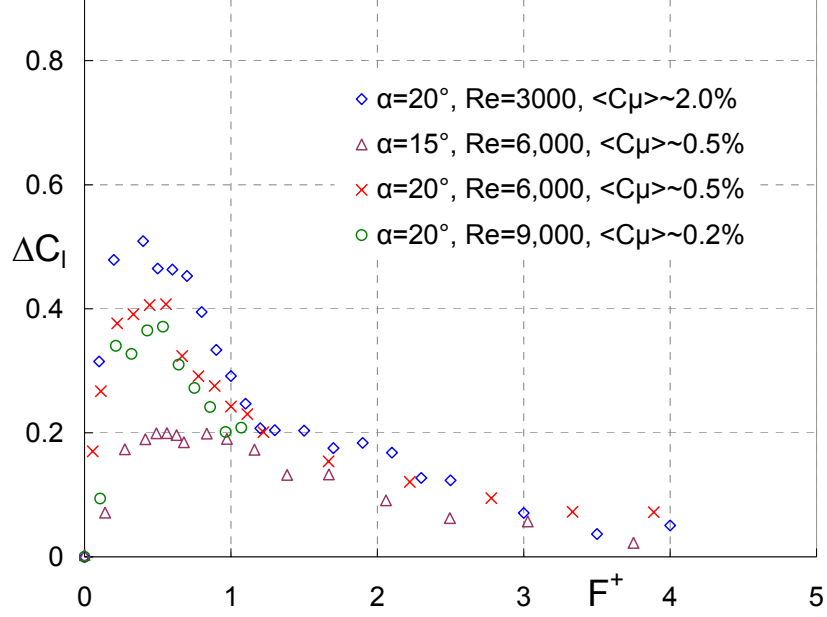


Fig. 4. Post-stall frequency scan at very low flight Reynolds numbers on the flat-plate airfoil, $DC=5\%$

4.1 Reduced Frequency Sensitivity

Corke et al. [5] observed, using pulsed plasma actuators, that the voltage (assumed proportional to $\langle C_\mu \rangle$) required to attach a post-stall separated flow was a minimum when F^+ was slightly larger than 1. Here, a systematic approach was adopted to determine the maximum post-stall C_l as a function of reduced frequency at various post-stall angles and Reynolds numbers (fig. 4). Selected representative smoke-wire visualization photographs are shown in figs. 5a to 5d. At all Re and $\alpha=20^\circ$, a maximum in C_l is evident at approximately $0.4 < F^+ < 0.6$; this is consistent with zero mass-flux blowing data acquired on a NACA 0015 at conventional low Reynolds numbers ($200,000 \leq Re \leq 600,000$). [7] However, at lower α , the peak extends to approximately 1. For a given α , the C_l changes are larger at the lower Re , where this is due primarily to the relatively larger $\langle C_\mu \rangle$ introduced by the actuator.

Flow visualization of the baseline case (fig. 5a) clearly shows separation from the leading-edge and subsequent rollup of the shear layer into distinct vortices. Flow separation from the trailing-edge appears to generate vortical structures with a longer wavelength. The difference between the flow over the stalled airfoil and control at $F^+=0.42$ is clearly seen by comparing figs. 5a and 5b. With control, the separated shear layer that detaches from the leading-edge rolls up into vortex (or bubble) that attaches to the airfoil surface. Downstream of this vortex, the previously generated vortex is in the process of being shed into the wake. A clockwise trailing-edge vortex can also be seen, presumably as a result of the low pressure now present on the plate upper surface. It is believed that the strong adverse pressure gradient existing on the upper surface of the airfoil is responsible for the dramatic upward distortion of the streamlines. Increases in control frequency produces rolled-up vortices successively closer to the leading edge (figs. 5b to 5d). For example, an increase in frequency by a factor of 5, to $F^+=2.1$ (fig. 5d), is only effective in transporting momentum towards the airfoil surface at $x/c < 0.1$. Immediately downstream of this, the small vortices are not effective in transporting high momentum fluid to the surface. Control at $F^+ < 0.1$ resulted in large lift and drag oscillations. These are consistent

with the generation of a leading-edge vortex that is shed into the wake before the following vortex is generated (cf. [17]). Lift oscillations are dramatically reduced when at least two vortices are present on the airfoil surface at any instant. Similar experiments were performed by driving the plasma actuators at 5kHz and similar aerodynamic results were obtained. The similarity between the present observations and biological flight at similar Reynolds numbers is discussed in section 4.3.

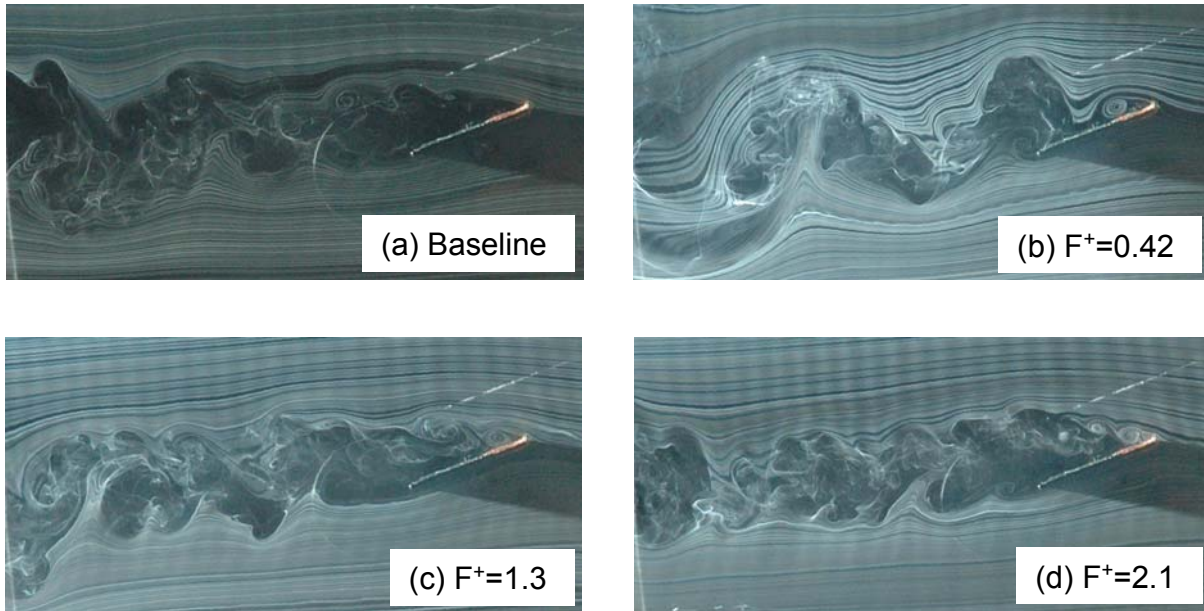


Fig. 5. Smoke visualization photographs corresponding to (a) baseline state; (b) optimum control; and (c,d) non-optimum control at $Re=3,000$, $\alpha=20^\circ$ (c.f. fig. 4).

It is instructive to compare the present data set with that acquired under similar conditions on the E338 airfoil [6] at $20,500 \leq Re \leq 50,000$ (Post stall $\alpha=14^\circ$ and 18°) and employing 3% and 5% duty cycles (fig. 6). At all reduced frequencies considered, there was a significantly larger positive effect on post-stall C_l . At the higher angle of attack ($\alpha=18^\circ$) the lift variation with frequency was mild, although an optimum was observed at $F^+ \approx 1.2$. Nevertheless, even at $F^+ \approx 10$, significant effects were observed and this is totally contrary to the flat plate observation where improvements were inconsequential for $F^+ > 3$ (c.f. figs. 4 and 6; same vertical scale). Moreover, at the lower angle ($\alpha=14^\circ$) the frequency dependency was more pronounced and again this observation was at odds with those of the flat plate.

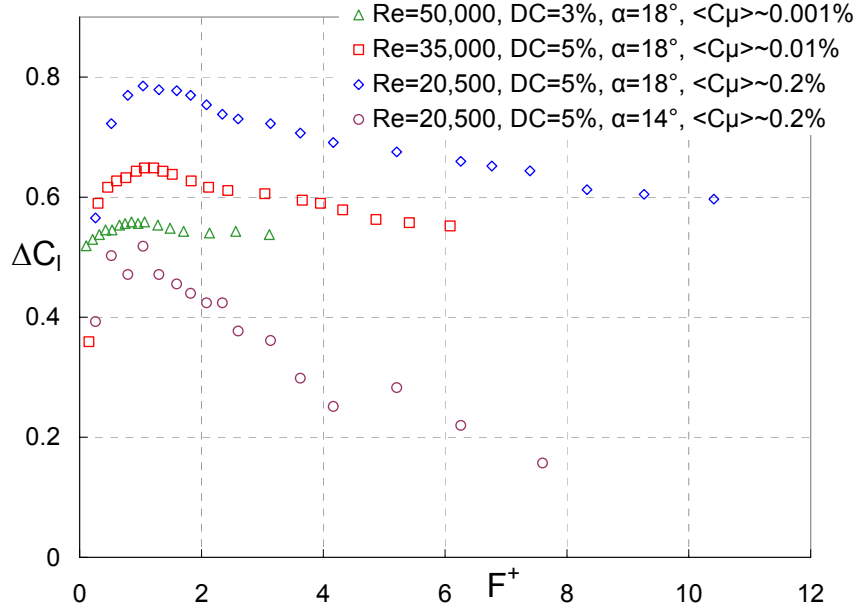


Fig. 6. Post-stall frequency scan on the Eppler E338 airfoil at low flight Reynolds numbers [6].

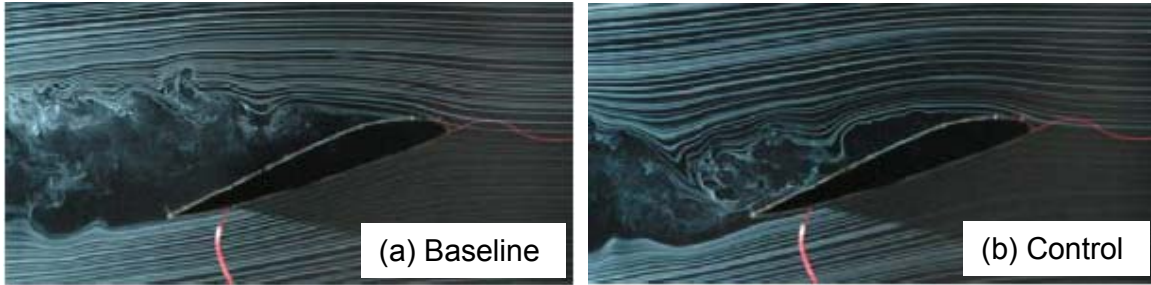


Fig. 7. Smoke visualization photographs corresponding to (a) baseline state; and (b) optimum control ($F^+=1.0$, 5% duty cycle). $Re=20,000$ and $\alpha=18^\circ$ (c.f. fig. 6) [6].

Post-stall flow visualization photographs for the E338 baseline and controlled scenarios (figs. 7a and 7b respectively) illustrate important differences between the two airfoils. More detailed experiments on the E338 can be found in [6]. With regard to the baseline state (cf. figs. 5a and 7a) we note that separation occurs at approximately $x/c=10\%$ on the E338 and the separation streamlines are closer to the airfoil surface than in the case of the flat plate. Also, the rollup of vortices observed at the leading-edge of the plate is absent on the E338, and this was also observed at $Re=10,000$ and $Re=6,000$. With perturbations introduced upstream of separation ($x/c=1\%$) the vortex generated has a larger aspect ratio, i.e. it is closer to the airfoil surface and is not as clearly defined as that on the flat plate (fig. 5b). Thus control in this case is more effective in turning the streamlines towards the airfoil surface and this results in higher lift. In addition, the dramatic upward distortion of the streamlines near the flat plate trailing-edge, associated with the downstream vortex, is not evident on the E338. It is a combination of these factors that lead to higher lift coefficients generated on this airfoil (cf. figs. 4 and 6). It is clear that details of the leading-edge geometry have a major effect on the efficacy and optimum frequency range of active flow control at very low flight Reynolds numbers.

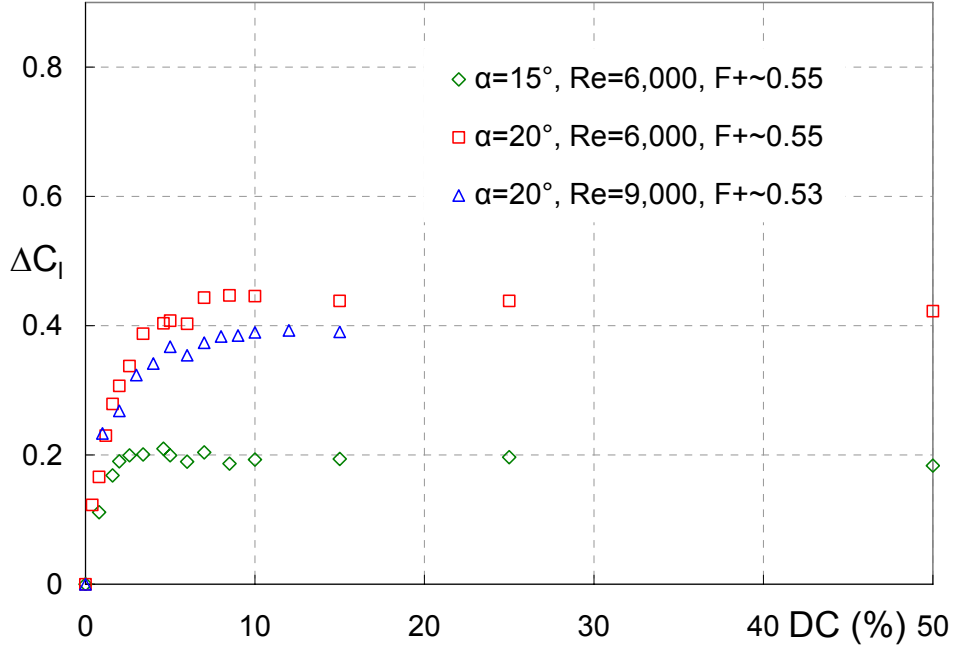


Fig. 8. Flat plate post-stall lift coefficient variation as a function of duty cycle.

4.2 Duty Cycle Dependence

As mentioned in section 2, wave modulation was employed such that the 4kHz carrier wave was modulated by a square-wave corresponding to low frequencies appropriate for separation control (cf. [8]). Thus the duty cycle (DC) was varied by changing the fraction of the square-wave period that the actuator was activated and this is expressed as a percentage. DC variations are shown in fig. 8 where data was acquired corresponding to the optimum reduced frequencies. All data, independent of α or Re show a relatively rapid increase in C_l with DC . At approximately $DC > 5\%$, the effect on lift is small with perhaps a gradual decrease as DC is increased beyond 10%. Figs. 1a and 1b provide an explanation for these observations. At $Re < 60,000$ and $DC = 5\%$, the oscillatory component of momentum lies mainly above the threshold necessary for control (fig. 1b). This explains the positive effect observed on lift irrespective of DC . The increase from $DC = 1\%$ to 5% results in a substantial increase in actuator momentum and this is primarily responsible for the larger increase in C_l observed here. An increase from $DC = 5\%$ to 10% does not bring about a significant difference in $\langle C_\mu \rangle$ and this is reflected in the small increase in C_l for this range. The increases in the steady momentum component are mostly below the threshold and thus play only a minor role (fig. 1a). Substantial increases in DC may result the threshold being exceeded but steady C_μ is still too small to play a meaningful role. There may be a slight deleterious effect (e.g. $DC = 50\%$) due to relatively low near wall momentum, which acts to promote boundary layer separation.

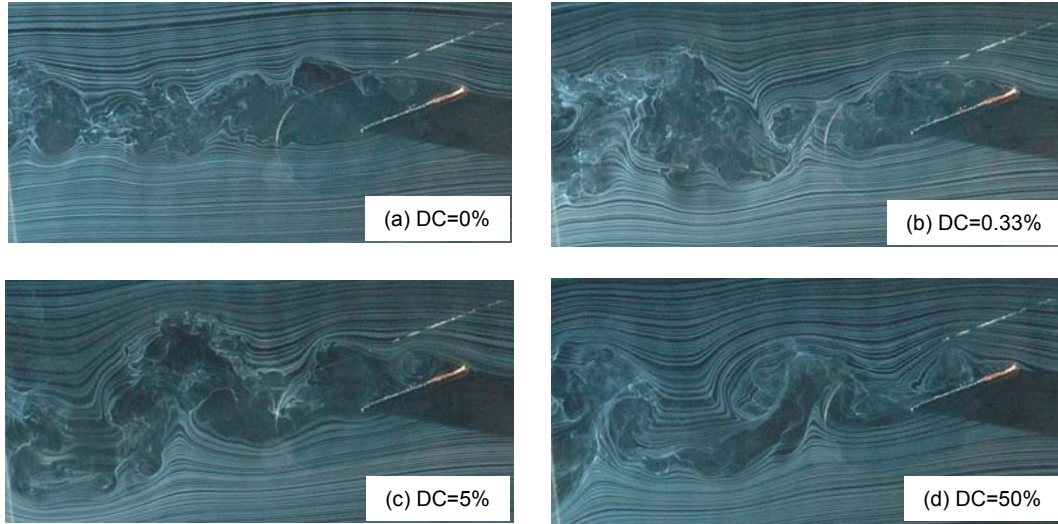


Fig. 9. Flat plate flow visualization at $F^+=0.46$ for varying duty cycle (indicated) with $Re=6,000$ and $\alpha=20^\circ$.

The flow visualization photographs shown in figs. 9a-9d add a qualitative dimension to these measurements. At $DC=0.33\%$ a small effect can be observed as the streamlines are deflected toward the plate upper surface (cf. figs 9a and 9b). However, there is no clear evidence of the formation of a leading-edge vortex. With an increase to $DC=5\%$ and 50% , a leading-edge vortex is clearly evident (figs. 9c and 9d).

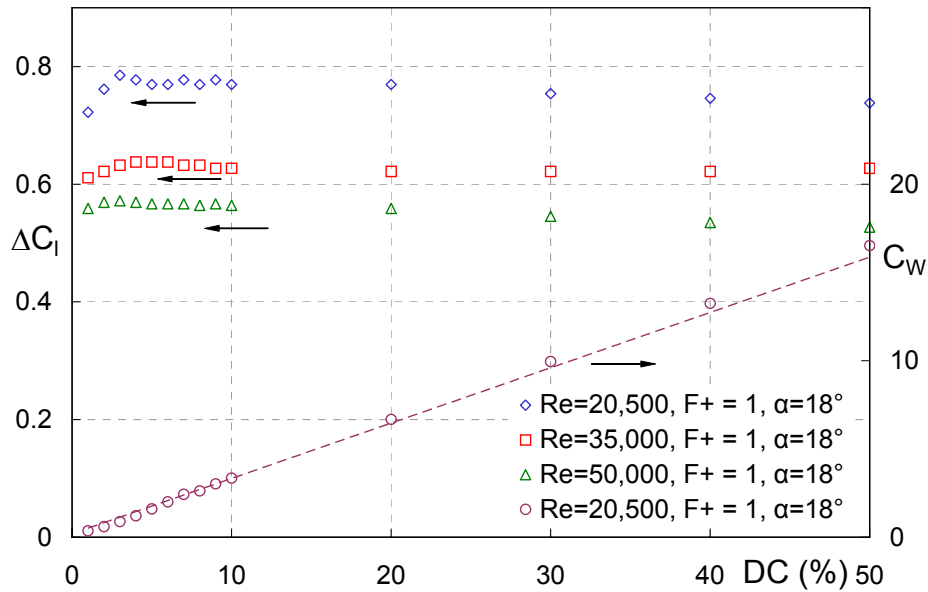


Fig. 10. Post-stall lift coefficient variation as a function of duty cycle on the Eppler E338 airfoil. [6]

Data acquired on the E338, close to its optimum reduced frequency ($F^+=1$), showed some generic similarities but also some very profound differences when compared to the flat plate (cf. figs. 10 and 8). A mild optimum was observed at in the approximate range $2\% < DC < 8\%$; as above, this is consistent with increases to the oscillatory momentum. However, the difference between the lift generated at optimum and non-optimum duty cycles differed by a small amount. In particular, as $DC \rightarrow 0$, there is only a small performance loss. The figure also shows the measured power, expressed as the power coefficient ($C_W \equiv W / \frac{1}{2} \rho U_\infty^3$), input to the actuator and emphasizes the important observation that similar performance benefits can be attained at a fraction of the power. With the power consumption reduced to 1.2mW/cm (0.66% duty cycle) $C_{l,max}$ did not drop significantly. At these duty cycles, however, the actuators could not be reliably calibrated and were estimated to produce $\langle C_\mu \rangle \sim 0.001\%$. Note that this is considered to be below the thresholds required for effective AFC. The small differences in performance are reflected in the flow visualization photographs taken at 1%, 5% and 50% duty cycle respectively (fig. 11).

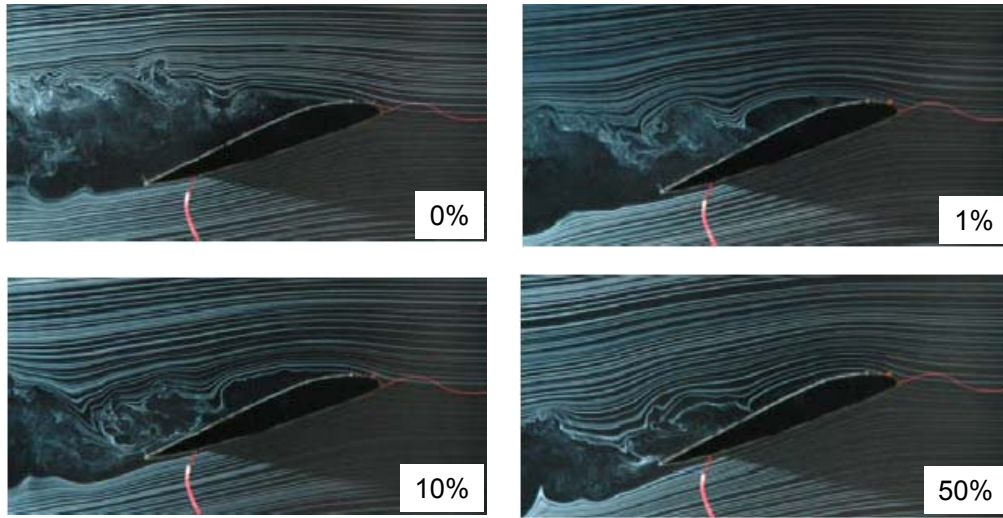


Fig. 11. Flow visualization on the Eppler E338 airfoil at $F^+=1.0$ for varying duty cycles (indicated), with $Re=20,500$ and $\alpha=18^\circ$ [6].

4.3 Performance Indicators & Control Mechanism

C_l versus α and C_l versus C_d polar plots are shown in figs. 12a-12d indicating the effect of control at four Reynolds numbers. In each instance, control is applied in the range that produced optimum post-stall C_l , namely $0.4 < F^+ < 0.6$. For illustrative purposes the data are discussed with respect to $Re=3,000$ and the corresponding description is provided with reference to figs. 13a-13j. Clearly, a similar description applies at the higher Reynolds numbers. At pre-stall angles of attack, typically $\alpha < 10^\circ$, control results in a reduction in lift. This is because the long bubble that exists naturally on the plate upper side is dramatically reduced or eliminated as a result of the perturbations. This can clearly be seen in the flow visualization photographs by comparing in fig. 13a and 13b, shown at $\alpha=6^\circ$. With increasing α , the bubble cannot enclose on the plate surface and “bursts” (fig. 13c). Control is seen to produce a long, relatively high-aspect ratio bubble on the upper surface, but no significant effects are seen on the wing lift or drag. Further increases in angle of attack ($\alpha=14^\circ$), result in complete separation from the upper

surface, accompanied by a significant drag rise. Control encloses a bubble near the leading-edge with an accompanying increase in lift and drag reduction. The bubble is shed downstream and, before it leaves the airfoil surface, a new bubble is generated near the leading edge. In the vicinity of $C_{l,max}$ ($\alpha \sim 20^\circ$), the same mechanism is observed, but the preceding vortex, that has traveled down the airfoil chord, is accompanied by significant deviation of the streamlines, indicating trailing-edge separation (fig. 13h). In deep post stall ($\alpha = 24^\circ$), control still produces the leading-edge vortex, but trailing-edge separation (fig. 13j) results in substantial loss of lift and drag increases.

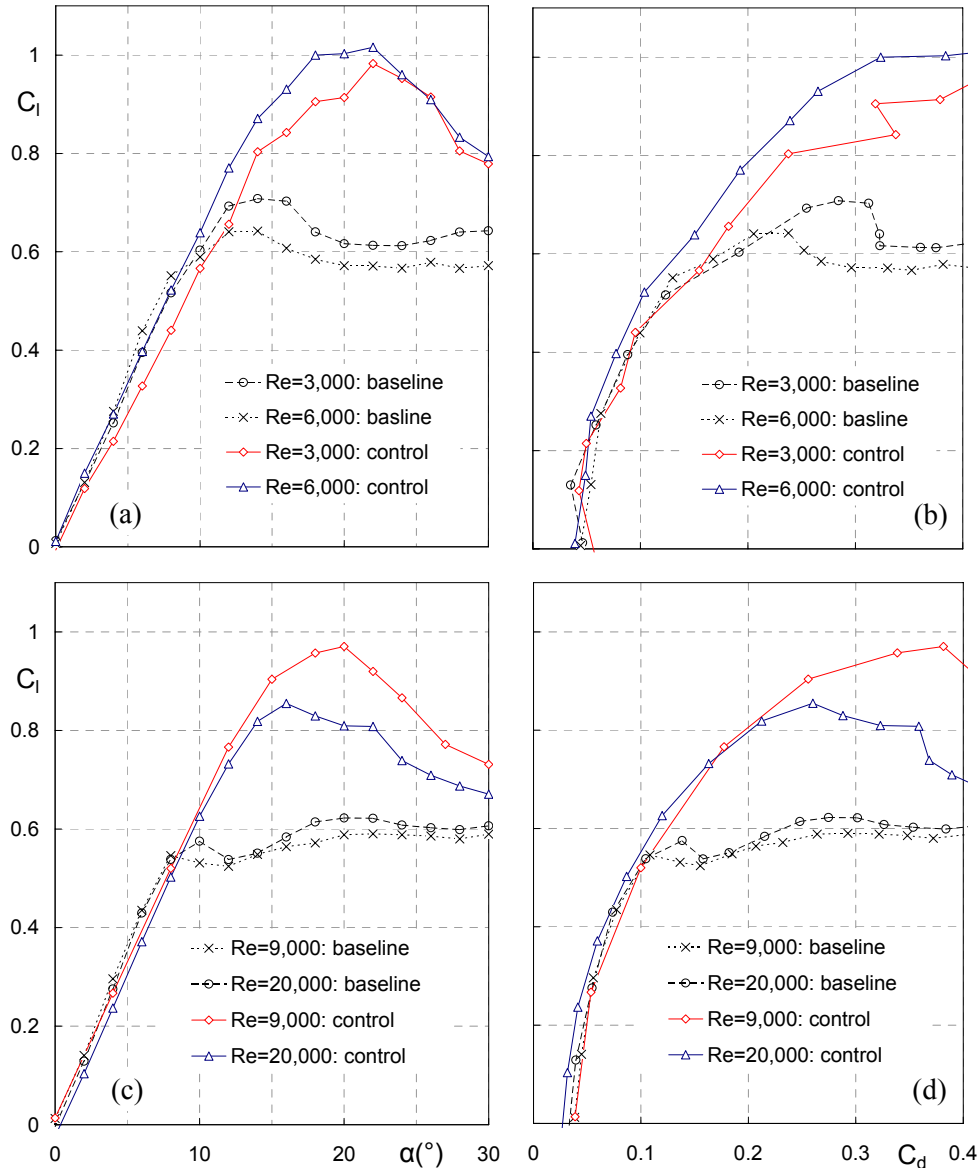
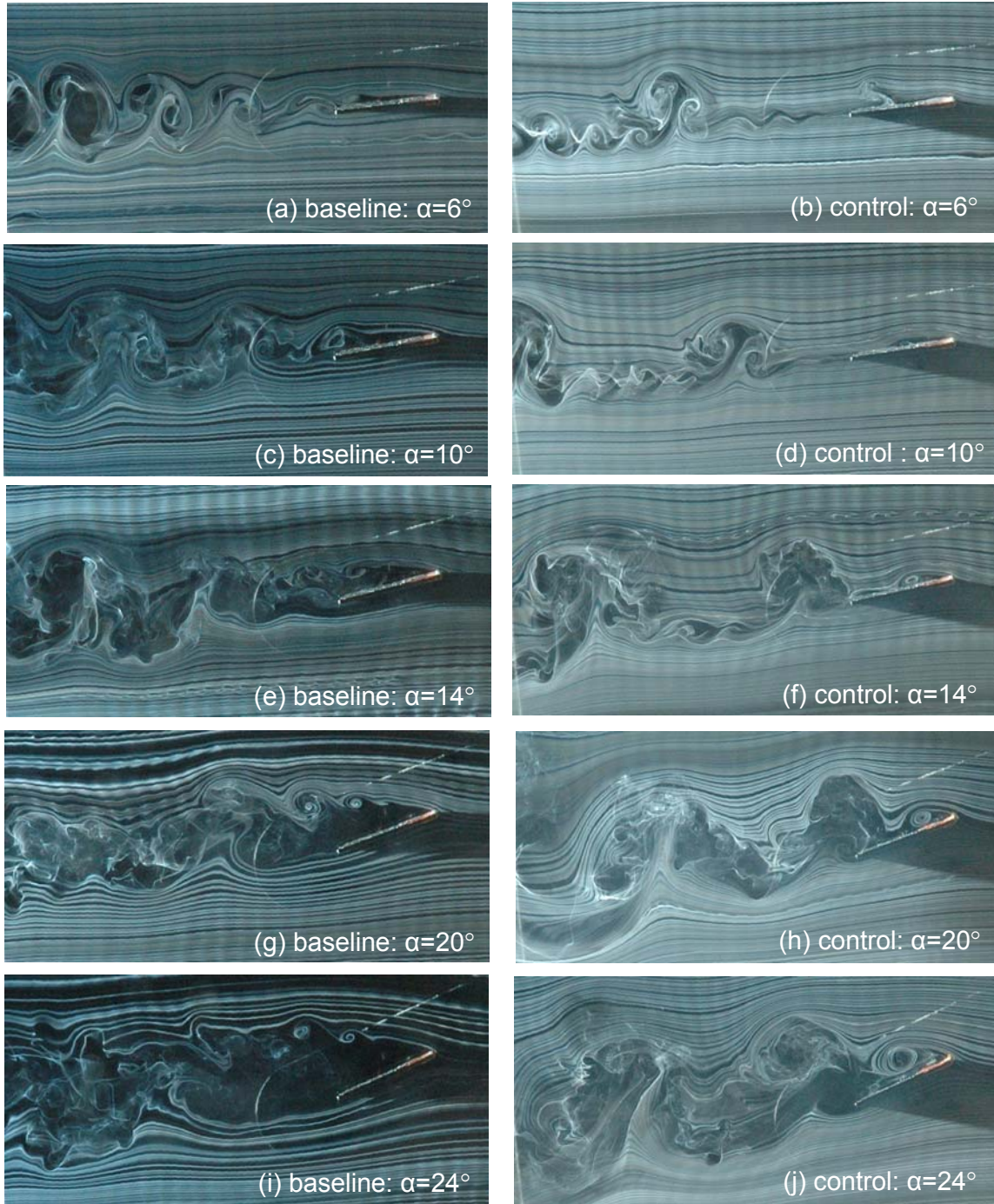


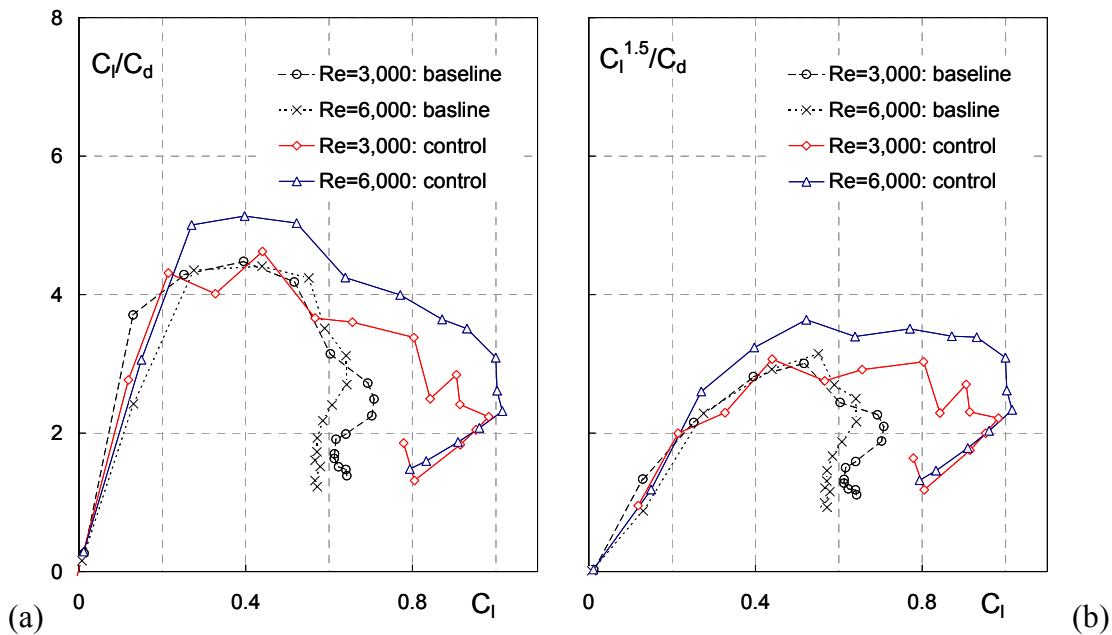
Fig. 12. Effect of control on the flat plate airfoil performance at typical NAV Reynolds numbers. Control at $0.4 < F^+ < 0.6$ and $DC=5\%$.



Figs. 13. Flow visualization of baseline (left-hand column) and optimum control (right-hand column; $F^+=0.42$, 5% duty cycle) at $Re=3,000$, for increasing angle of attack.

It is well known that small flying creatures, whose wings generate useful lift at these Reynolds numbers, remain airborne by means of at least one unsteady flow mechanism. [13-16] One such mechanism is the so-called “separation bubble” or vortex, which forms during the downstroke of the wing, and generates the high lift required for flight. This bubble is similar to the well-known dynamic stall vortex (DSV) that is observed on oscillating airfoils. Control of the

DSV has received considerable attention due to its association with dynamic stall on rotor blades and wind turbines. [17] The apparent paradox that the DSV generates very large oscillations in lift but is at least partially responsible for the flight for small creatures can be resolved as follows. From the statistical data summarized by [13], for the NAV range the typical reduced frequencies associated wing flapping are $0.1 \leq F^+ \leq 1$ (in hover $F^+ \rightarrow \infty$). This should be contrasted with equivalent reduced frequencies associated with oscillating helicopter rotor blades, namely $0.015 \leq F^+ \leq 0.05$. Thus some flying creatures can generate “dynamic stall vortices” at a rate high enough to ensure sustained flight, i.e. at least one vortex will always be present on the upper surface of the wing or body at any instant. A similar explanation can be given for active flow control introduced here, where there are typically 2 vortices present on the airfoil at any instant. This ensures stable, as well as effective, lift since the excitation-generated vortices do not bring about large variations in aerodynamic loads. [18]



Figs. 14. (a) Efficiency parameter and (b) endurance parameter for the flat plate airfoil (control at $F^+ \sim 0.4$, 5% duty cycle).

The aforementioned performance improvements result in modest gains to the airfoil efficiency parameter C_l/C_d (figs. 14a and 15a). The low efficiency throughout the α range, for both baseline and control scenarios, is a consequence of the high viscous drag associated with low Reynolds numbers, and the large upper surface bubble. These sources of drag may be unavoidable at these low Reynolds numbers. Somewhat better results are obtained by the endurance parameter, $C_l^{1.5}/C_d$ (figs. 14b and 15b). Here, the same or greater endurance can be achieved at up to two times the lift coefficient. This is of importance for mission-critical loitering-flight where a combination of low flight speeds (high C_l) and high endurance is often desirable. As expected, there is an increase in both baseline and control efficiency and endurance parameters with increasing Reynolds number (cf. figs. 14a and 15a).

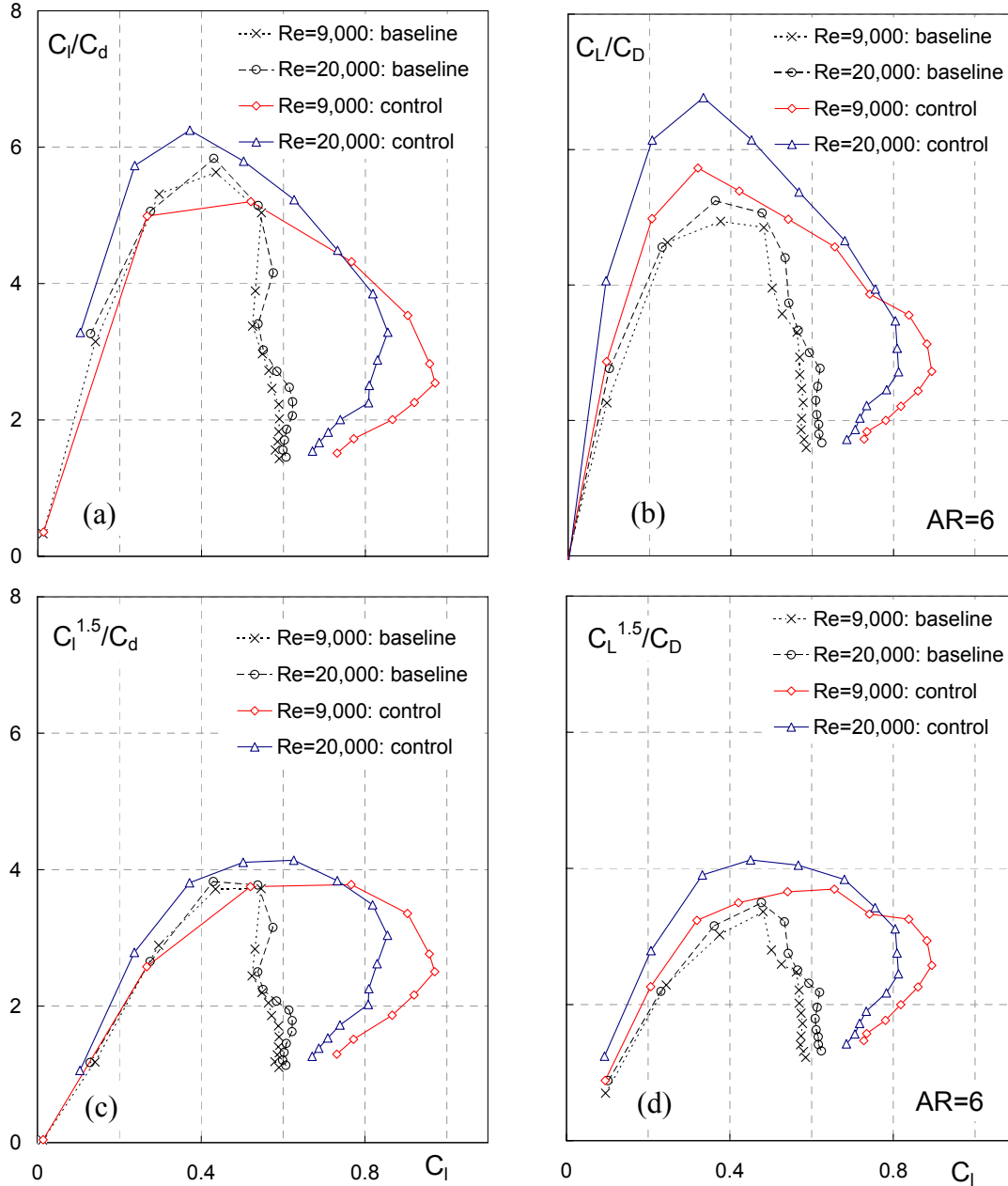
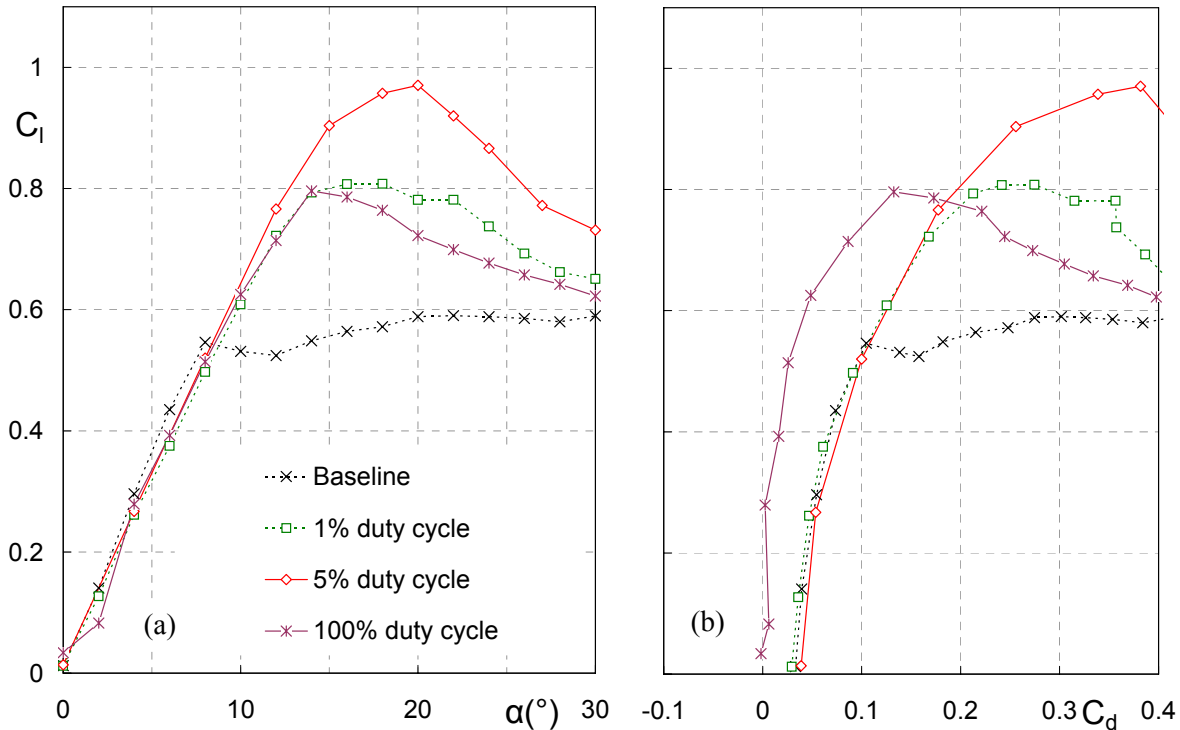


Fig. 15. Flat plate efficiency and endurance parameters for the (a,c) airfoil and (b,d) semi-span wing ($0.4 < F^+ < 0.6$, 5% duty cycle).

Removal of the lower end-plate produced a semi-span wing with $AR=6$, discussed previously with reference to fig. 2b. A comparison of the efficiency parameter for the two-dimensional configuration and the semi-span configurations (figs. 15a and 15b) shows, as expected, that the baseline $(C_l/C_d)_{\max}$ exceeds $(C_L/C_D)_{\max}$ due to induced drag. However, the same indicators associated with control do not show this trend and there is even a small increase on the finite wing. Similar observations can be made with respect to $C_l^{1.5}/C_d$ and $C_L^{1.5}/C_D$ (cf. fig. 15c and 15d). It is conjectured that actuation near the tip of the wing, modifies the shed vorticity in this region so as to reduce induced drag.

4.4 Steady Control – 100% Duty Cycle

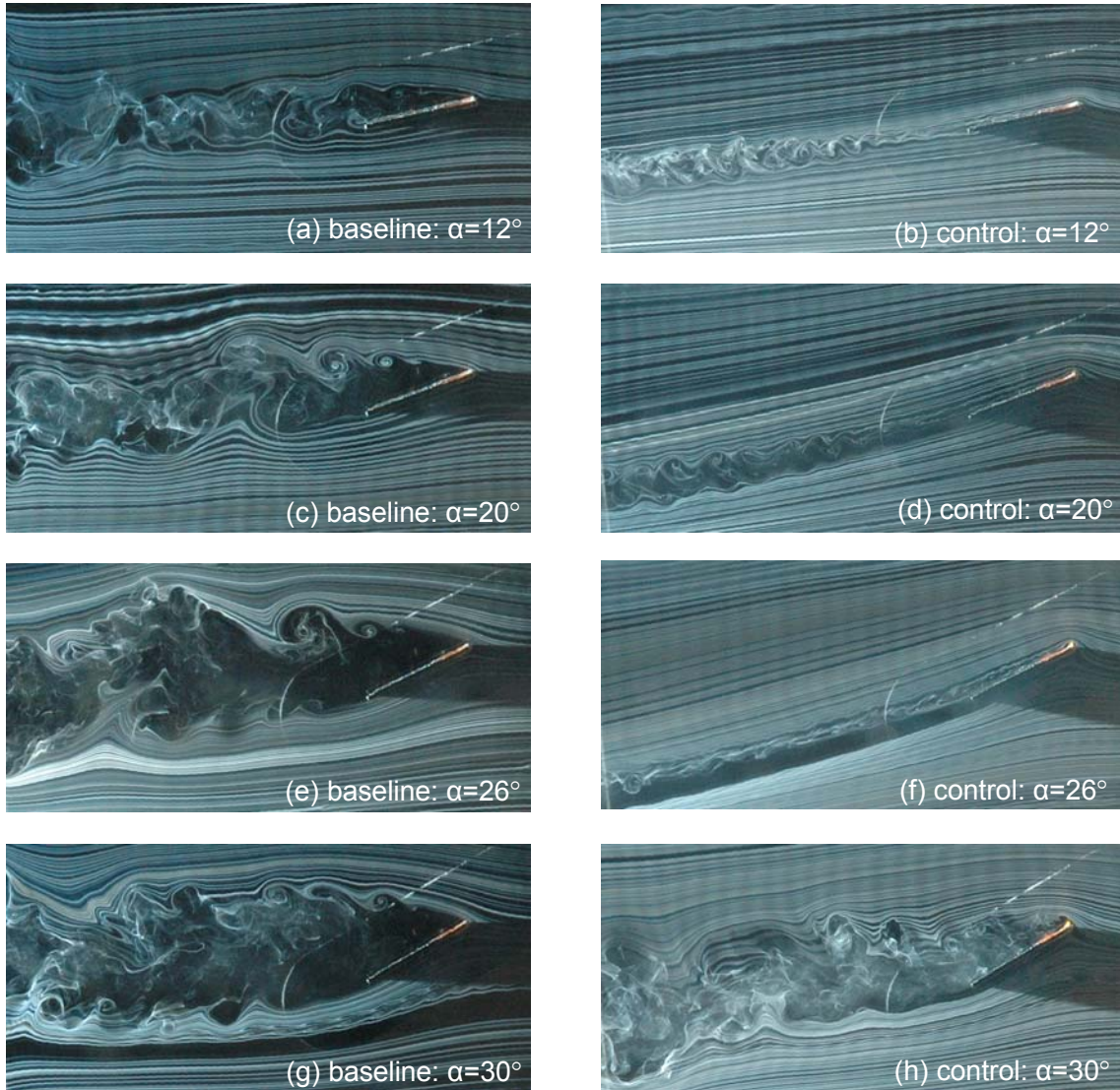
Historically, steady slot blowing was employed as an effective means of boundary layer control, but it was abandoned mainly due to design complexity and heavy plumbing systems. At very low flight Reynolds numbers, an analogy to steady blowing can be achieved using DBD actuators, where the actuators are not pulsed, i.e. they are driven at $DC=100\%$. It is generally assumed that the flow does not respond to the high-frequency oscillations, presently 4kHz, and the flow can be considered as a “steady” jet. Returning to fig. 1, and considering the momentum coefficient calibration for $DC=100\%$, it is evident that “steady” control may only be applicable in the extremely low flight Reynolds number range, namely $Re < 30,000$.



Figs. 16. Flat plate airfoil performance at various duty cycles. Pulsed control at $F^+=0.55$.

Attempts were made to measure the lift and drag forces at $Re=3,000$ and $6,000$, but the combination of high instrumentation sensitivity and strong electromagnetic radiation produced by the actuator resulted in unacceptably high noise levels, thereby precluding meaningful measurements. Thus, only flow visualization was performed at these Reynolds numbers (discussed below). However, at $Re=9,000$, the SNR was sufficiently improved to facilitate measurements at $DC=100\%$ and the results are shown in figs. 16a and 16b. The graphs also contain data for 1% and 5% duty cycle. At $\alpha=0^\circ$, it is evident that steady blowing slightly increases lift due to an increase in circulation produced by the effectively steady jet. The jet also effectively eliminated drag; $C_{\mu} = 0.076$ is required to overcome $C_{d0}=0.033$. Thus it may be concluded that on this configuration, at $Re < 9,000$, steady control effectively produces thrust. With increasing pre-stall angles, steady control has a similar effect to of pulsed control and it is therefore assumed that the bubble is similarly reduced or eliminated. However, with further increase into the post-stall regime, steady control is approximately as effective as 1% duty cycle control in terms of $C_{l,max}$, although the corresponding drag is substantially lower, but inferior to

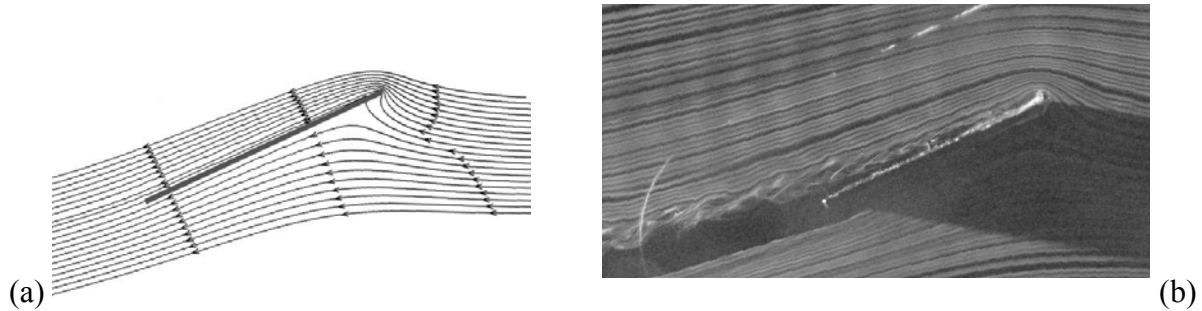
$DC=5\%$ pulsing. It is assumed that with increasing angle of attack, the high-speed flow velocity accelerating around the leading edge eventually exceeds that produced by the steady jet. Consequently, the near wall momentum is sufficiently depleted and the airfoil stalls. These data serve to illustrate the important differences between effectively “steady” control and the exploitation of unsteady lift-generation mechanisms.



Figs. 17. Flow visualization of baseline (left-hand column) and “steady” control (right-hand column; 4kHz, 100% duty cycle) at $Re=3,000$, for increasing angle of attack.

Although direct force measurements could not be made at the lower Reynolds numbers, smoke flow visualization was used to provide a qualitative description of the flow. Baseline and control photographs at several post-stall angles are shown in figs. 17a-17h for $Re=3,000$. Based on the calibration shown in fig. 1 and the results shown in fig. 16b, it is clear that steady control produces thrust at low α because $C_{d0}=0.044$ versus $C_{\mu} = 0.68$. It can be assumed that most of the momentum produced by the actuator is recovered as thrust, although this was not directly

measured. At the post-stall angles shown in the figures, it is clear that steady blowing dramatically eliminates separation by producing a high-speed jet adjacent to the surface. This can be achieved up to $\alpha=26^\circ$. The stall mechanism at $\alpha>26^\circ$ is similar to that described above.



Figs. 18. (a) Streamlines generated by means of the potential flow solution around a flat plate [19]; (b) smoke visualization of “steady” control (at 4kHz, 100% duty cycle). $Re=3,000$ and $\alpha=26^\circ$.

A comparison of the streamlines generated by steady blowing with those of a potential flow about a flat plate are shown in figs. 18a and 18b. Details of the visualized streamlines, particularly in the leading-edge region, correspond well with potential flow theory. However, the upper surface flow is seen to separate at approximately $x/c=20\%$ and the separated region grows to a substantial fraction of the chord length. Based on extrapolation of the data shown in fig. 16, it should not be expected that $C_{l,max}$ will exceed 1.6 at $\alpha=26^\circ$.

4.5 Control of the Airfoil Wake

At pre-stall angles of attack, it was observed that α has a significant effect on the wake stability and structure. At $\alpha=0^\circ$, the flow on both surfaces separates at the blunt trailing-edge and the streamlines smoothly merge at approximately $x/c=10\%$ downstream of the trailing-edge. The wake is seen to undergo an instability downstream of the trailing-edge that evolves into a series of alternately signed vortices, similar to a Kármán vortex street observed immediately downstream of bluff bodies (fig. 19a). If we assume that the vortices’ velocity is $O(U_\infty)$, then this corresponds to F^+ that is based on the number of vortices present over a one chord-length distance. Consideration of the fully rolled vortices (fig. 19a) indicates that $F^+ \sim 2.2$. Small increases in angle of attack ($\alpha=2^\circ$; fig. 19b) produce an asymmetric wake structure with a larger overall transverse width, but the distance between the structures is not affected. Further increases ($\alpha=4^\circ$; fig. 19c) produce the same trend while the rollup of the vortices occurs closer to the trailing-edge, and the inter-structure distance still remains the same. Up to this angle, the wavelength between the structures does not vary appreciably. As the airfoil approaches incipient stall ($\alpha=6^\circ$; fig. 19d), the upper surface bubble is seen to be shedding into the wake and interacting directly with the vortex shed from the lower surface. This has significant consequences for the wake: (a) formation of the vortex structure now occurs immediately downstream of the airfoil trailing-edge; (b) the transverse extent of the wake increases dramatically, while its basic structure remains the same; (c) the wavelength between structures is approximately doubled. Further α increases, to post-stall angles, dramatically alters the vortex shedding mechanisms (see fig. 13).

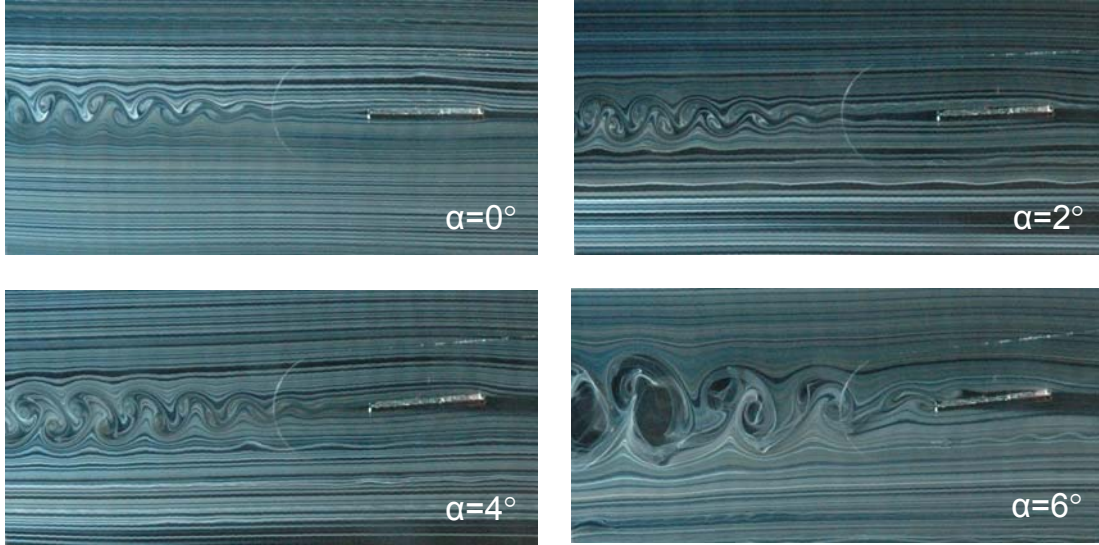


Fig. 19: Flow visualization photographs of flow over the airfoil and in its wake at increasing pre-stall angles of attack ($Re=3,000$).

Forcing the flow at incipient stall ($\alpha=6^\circ$) has further significant effects on the wake structure. To illustrate this, flow visualization photographs are shown for 5% duty cycle where the pulsing frequency was varied from 8 to 54 Hz, corresponding to $F^+=0.5$ to 3. Small reductions in C_l , resulting from control (e.g. fig. 12a) are measured under these conditions due to the reduction of the bubble size. Forcing at $F^+=0.5$ (fig. 20a) shows a significant effect on the bubble, and a single structure is observed extending approximately $x/c=25\%$ above the plate upper surface. It seems that this structure produces two significant effects on the wake: (a) the first rolled up structure evident immediately downstream of the trailing-edge in the baseline case now forms at approximately $1\frac{1}{2}$ chord-lengths downstream of the trailing-edge; (b) instead of regularly spaced structures, the wake is now composed of a larger structure interposed with smaller, mainly clockwise rotating structures. The apparent reason for this is that the natural shedding frequency from the upper surface ($F^+\sim 2.2$) is now regulated to shed at $F^+=0.5$, while the lower surface shedding still occurs at $F^+\sim 2.2$. This results in multiple (~ 4) clockwise vortices, whose inter-vortex spacing is comparable to that at $\alpha=0^\circ$ (fig. 19a), being shed for each counter-clockwise vortex as shown in fig. 20a. Doubling the forcing frequency ($F^+=1.0$; fig. 20b) results in the rolled up wake structure moving closer to the airfoil trailing-edge, where each conventional wake structure is now interposed by a single clockwise rotating structure. This consistent with the above explanation where now two clockwise vortices are shed for each counter-clockwise vortex. Further increases in frequency produce multiple vortices on the plate upper surface. The wake behavior remains consistent with our physical description, and at frequencies comparable to the shedding frequency (figs. 20c and 20d), the wake regains the structure observed at $0^\circ\leq\alpha\leq 4^\circ$. Indeed the spacing between vortices at these low angle of attack is between those observed at $F^+=2.0$ and 3.0 (figs. 20c and 20d).

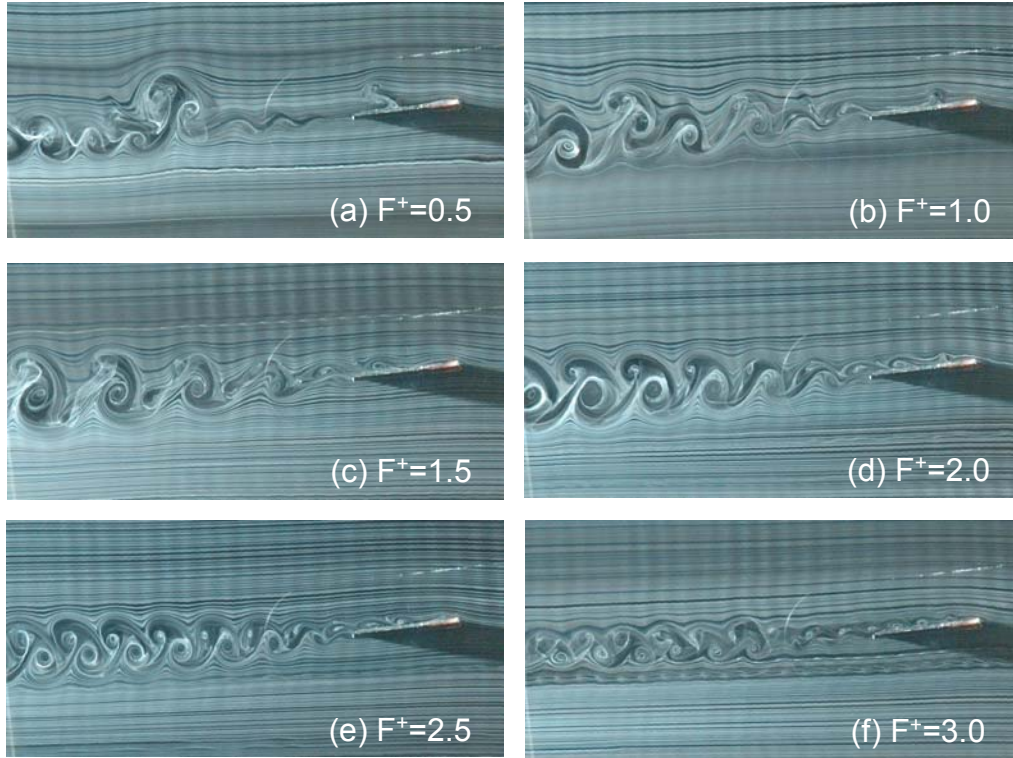


Fig. 20: Flow visualization photographs of flow over the airfoil and in its wake for increasing control reduced frequencies ($DC=5\%$; $\alpha=6^\circ$, $Re=3,000$).

5. CONCLUSIONS

Active flow control, employing a dielectric barrier discharge plasma actuator, was studied on a flat plate airfoil and a semi-span wing for $3,000 \leq Re \leq 20,000$. Selected data was compared with that of an Eppler E338 airfoil. The following main conclusions were drawn:

1. Pulsed-mode actuation at post-stall angles of attack revealed that maximum lift coefficients were generated in the reduced frequency range $0.4 < F^+ < 0.6$, with a sharp drop in lift at higher F^+ . These data were consistent with NACA 0015 data acquired at 200 times the Reynolds number [7], but differed from the low Re E338 airfoil data [6], which showed a relatively mild dependence on F^+ .
2. Duty cycles greater than 5% were found to produce maximum lift due to the relatively large $\langle C_\mu \rangle$ produced in this DC range. The E338 airfoil lift, however, was nearly insensitive to duty cycle.
3. Actuation produced an increase in increase in $C_{l,max}$ of up to 0.4 and similar order of improvements to post-stall C_l . These changes did not match those of the E338 (post-stall $\Delta C_l > 0.55$) and it was concluded that leading-edge geometry has a profound effect on active flow control efficacy at these Reynolds numbers.
4. Actuation maintained an elevated endurance parameter at significantly higher lift coefficients.
5. Control-based performance enhancements observed on the semi-span wing were slightly superior to those observed on the airfoil. This was assumed to be due to tip vortex modification resulting from actuation near the tip.

6. Actuation in the “steady” mode allowed control up to 26° angle of attack and thrust was produced at $Re < 9,000$.
7. Control actuation exerted a significant effect on the wake at pre-stall angles of attack, where control of the upper surface bubble shedding produced significant differences in wake spreading and inter-vortex spacing.

This investigation mainly illustrated the significant effects of DBD actuation at very low flight Reynolds numbers employing both steady and pulsed control. The comparison of different airfoil performance indicators clearly demonstrated the impact of leading-edge detail on the efficacy of active control. A further study, of a similar nature, is recommended to introduce the effect of curvature via airfoil camber.

REFERENCES

1. Mueller T.J., “Aerodynamic Measurements at Low Reynolds Numbers for Fixed Wing Micro-Air Vehicles,” Presented at the RTO AVT/VKI Special Course on Development and Operation of UAVs for Military and Civil Applications, VKI, Belgium, September 13-17, 1999.
2. Nagel, A., Levy, D.E. and Shepshelovich, M., “Conceptual Aerodynamic Evaluation of MINI/MICRO UAV,” AIAA Paper 2006-1261, 44th Aerospace Sciences Meeting and Exhibit, 9-12 January 2006, Reno, NV, 2006.
3. Nano Air Vehicle Program. www.darpa.mil/dso/solicitations/BAA06-06_sect2.pdf, 2006.
4. Roth, J.R., Sherman, D. and Wilkinson, S., “Boundary Layer Flow Control with One Atmosphere Uniform Glow Discharge Surface Plasma,” AIAA 1998-0328, 1998.
5. Corke, T.C. He C. and Patel, M.P., “Plasma flaps and slats: An application of weakly ionized plasma actuators,” AIAA Paper 2004-2127, 2nd AIAA Flow Control Conference, Portland, Oregon, 2004.
6. Göksel, B. Greenblatt, D., Rechenberg I., Nayeri, C.N. and Paschereit, C.O., “Steady and Unsteady Plasma Wall Jets for Separation and Circulation Control,” AIAA Paper 2006-3686, 3rd AIAA Flow Control Conference, San Francisco, CA, 5-8 June 2006.
7. Seifert, A., Darabi, A. and Wygnanski, I., “Delay of airfoil stall by periodic excitation”, AIAA Journal of Aircraft, Vol. 33, No. 4, 1996, pp. 691-698.
8. Greenblatt, D and Wygnanski, I., “The control of separation by periodic excitation,” Progress in Aerospace Sciences, Volume 37, Issue 7, 2000, pp. 487-545.
9. Poisson-Quinton, Ph. and Lepage, L., “Survey of French research on the control of boundary layer and circulation,” in Lachmann, G. V., “Boundary layer and Flow Control. Its Principles and Application”, Volume 1, Pergamon Press, New York, 1961, pp. 21-73.
10. Attinello, J.S., “Design and Engineering Features of Flap Blowing Installations”. In G.V. Lachmann, “Boundary Layer and Flow Control. Its Principles and Application”, Volume 1, 1961, Pergamon Press, New York, pp. 463-515.
11. Schmitz, F.W., ‘Aerodynamik des Flugmodells, Tragflügelmessungen I’, C.J.E. Volckmann Nachf. E. Wette, Berlin-Charlottenburg, 1942.
12. Roth, J. R. and Dai, X. (2006) Optimization of the Aerodynamic Plasma Actuator as an Electrohydrodynamic (EHD) Electrical Device. AIAA Paper 2006-1203, 44th AIAA Aerospace Sciences Meeting and Exhibit, Reno, Nevada.
13. Shyy, W., Berg, M. and Ljungqvist, D., “Flapping and Flexible Wings for Biological and Micro Air Vehicles”, Progress in Aerospace Sciences, Vol. 35, Issue 5, 1999, pp. 455-505.

14. Pornsin-Sirirak, T., Lee, S. W., Nassef, H., Grasmeyer, J., Tai, Y. C., Ho, C. M. and Keennon, M., "MEMS Wing Technology for a Battery-Powered Ornithopter", Thirteenth IEEE International Conference on Micro Electro Mechanical Systems (MEMS '00), Miyazaki, Japan, Jan. 23-27, 2000.
15. Maxworthy, T., "The Fluid Dynamics of Insect Flight", *Ann. Rev. Fluid Mech.*, Vol. 13, 1981, pp. 329-50.
16. Spedding, G. R. and Maxworthy, T., "The Generation of Circulation and Lift in a Rigid Two-Dimensional Fling", *J. Fluid Mech.*, Vol. 165, 1986, pp. 247-272.
17. Carr, L. W., "Progress in the Analysis and Prediction of Dynamic Stall" *AIAA Journal of Aircraft*, Vol. 25, No. 1, 1988, pp. 6-17.
18. Greenblatt D. and Wygnanski, I., "Use of Periodic Excitation to Enhance Airfoil Performance at Low Reynolds Numbers," *AIAA Journal of Aircraft*, Volume 38, Issue 1, 2001, pp. 190-192.
19. Albrecht, T., "Aerodynamik Aufgabensammlung," TU Dresden, 12.2006.